Exospheric distributions of minor ions in the solar wind

V. Pierrard, H. Lamy, and J. Lemaire
Belgian Institute for Space Aeronomy, Brussels, Belgium

Received 2 June 2003; revised 4 December 2003; accepted 5 January 2004; published 27 February 2004.

[1] We investigate the acceleration of heavy solar wind ions on the basis of an exospheric Lorentzian model and show that the heavy ions can flow faster than the protons when their temperatures in the corona are more than proportional to their mass. The Lorentzian kinetic exospheric model [*Pierrard and Lemaire*, 1996], initially developed only for electrons and protons of the solar wind in a monotonic potential energy, is here generalized for the case of a nonmonotonic potential energy and applied to the heavy solar wind ions. We study how the mass, the charge, and the coronal temperature of the heavy ions influence their motion. The present work indicates that the temperature of the ions in the corona characterizing the dispersion of their velocities is a crucial factor determining their bulk velocity at large radial distances. *Pierrard and Lamy* [2003] showed that the velocity filtration effect can produce very high values of ion temperatures in the solar corona, considering that ion velocity distribution functions are enhanced with suprathermal tails in the low corona. We show that for sufficiently high ion temperatures at the exobase, our exospheric model can account for large bulk speeds of the heavy solar wind ions and for their relative abundances at 1 AU. *INDEX TERMS:* 2164 Interplanetary Physics: Solar wind plasma; 2169 Interplanetary Physics: Sources of the solar wind; 7511 Solar Physics, Astrophysics, and Astronomy: Coronal holes; 7509 Solar Physics, Astrophysics, and Astronomy: Corona; 2118 Interplanetary Physics: Energetic particles, solar; *KEYWORDS:* solar wind, ion acceleration, exospheric model, kappa distribution, velocity filtration

Citation: Pierrard, V., H. Lamy, and J. Lemaire (2004), Exospheric distributions of minor ions in the solar wind, *J. Geophys. Res.*, *109*, A02118, doi:10.1029/2003JA010069.

1. Introduction

[2] Not only electrons and protons escape from the solar corona; traces of heavier elements have been identified. An average of 95% of the solar wind ions are protons. Helium is the most abundant heavy ion with 3.2% in average in the slow solar wind and 4.2% in the high speed solar wind [*Schwenn*, 1990]. However, this fraction is variable, especially in the slow speed solar wind, and helium concentration can sometimes be as high as 10% of the total ions concentration. Oxygen, carbon, neon, nitrogen, silicon, magnesium, iron, sulfur, and other heavy minor ions are also detected in much smaller amounts (around 1% all together). The characteristics of these heavy solar wind ions in different ionization states are better and better known from new spacecraft particle measurements [*von Steiger et al.*, 1995] and ultraviolet coronal spectroscopy [*Kohl et al.*, 1997].

[3] The velocity distribution functions (VDF) of solar wind heavy ions have been measured at 1 AU by accumulation of counts over long time periods due to their small densities and fluxes. They are generally non-Maxwellian and characterized by an excess of fast particles that have a power law energy spectrum. Such distributions can conveniently be fitted by "Kappa" (or generalized Lorentzian) functions where the κ index determines the slope of their suprathermal energy distribution. The larger the value of κ, the lesser the excess of suprathermal particles. The VDFs of solar wind neon, oxygen, and helium ions determined from WIND observations have been fitted with kappa distributions; the values of the κ index range between 2.5 and 5 [*Collier et al.*, 1996]. Electron VDFs measured by ULYSSES have also significant non-Maxwellian suprathermal tails with κ ranging between 2 and 7 [*Maksimovic et al.*, 1997b].

[4] ULYSSES observations in the high-speed solar wind indicate that the kinetic temperatures T_i of the heavy ions are much larger than the proton temperature, T_p; T_i/T_p is larger than their mass ratio m_i/m_p [*von Steiger et al.*, 1995]. Moreover, at 1 AU in the high-speed solar wind, the bulk velocities of the heavy ions are often equal or larger than the proton bulk velocity by a few percent [*Ogilvie et al.*, 1982; *von Steiger et al.*, 1995].

[5] Spectroscopic measurements of emission lines in the corona show that even at low altitude (between 1.05 and 5 Rs), solar wind helium and heavy ions are not in thermal equilibrium with the protons. The Doppler broadening of spectral lines emitted by highly ionized ions indicates very high ion temperatures at the base of the solar corona. Recent observations of spectral lines carried out with UVCS spectrometer on board SOHO indicate that the temperature of the protons is around 2×10^6 K at 2.8 Rs in the corona and that the temperature of the ions O^{5+} can be as high as

0148-0227/04/2003JA010069

$T_{O^{5+}} = 2.5 \times 10^8$ K [*Esser et al.*, 1999]. For Mg^{9+}, these authors found 6×10^7 K at 2 Rs. The outflow velocity of the ions O^{5+} is also determined from UVCS spectral line profiles; it is found to be twice that of the protons at this low heliographic radial distance [*Cranmer et al.*, 1999]. All these features confirm that the coronal plasma is not in thermal equilibrium.

[6] The conventional mechanisms proposed to heat the corona and accelerate the solar wind electrons and protons (such as heating by current sheets or dissipation by acoustic wave (see *Parker* [1991] for a review)) cannot explain the high temperatures and the acceleration of the minor ions observed in the corona. Therefore an additional specific process has been proposed to explain the unexpected high temperatures and bulk velocities of the heavy ions: the dissipation of ion-cyclotron resonant Alfvén waves.

[7] Recently, an alternative theory was proposed by *Pierrard and Lamy* [2003]: the velocity filtration effect. This mechanism was initially suggested by *Scudder* [1992a, 1992b] to explain the inversion of the coronal temperature profile in the solar atmosphere. This mechanism is based on the assumption that particle velocity distribution functions with enhanced suprathermal tails can "heat" the corona by increasing the ratio of suprathermal over thermal particles as a function of altitude, without deposition of wave or magnetic field energy into the gas [*Dorelli and Scudder*, 1999]. When applied to the minor ions of the solar wind, the velocity filtration effect implies ion temperatures T_i in the low corona which are more than proportional to the ion mass. The mechanism of velocity filtration predicts very broad velocity distributions for coronal ions and T_i increasing with altitude in the lower regions of the corona.

[8] The aim of the present study is to include minor ions in kinetic exospheric models and investigate the influence of high ion temperatures on the acceleration of the solar wind ions. In the first section, we describe the generalization of the exospheric kappa model to the case of a nonmonotonic distribution of total potential energy, as it happens for the solar wind heavy ions. In the second section, we apply the model to the minor ions to obtain their number densities, bulk velocities, and temperatures profiles. Then we discuss the results and the influence of the different parameters. Conclusions are provided in the last section.

2. Lorentzian Exospheric Model

[9] Kinetic collisionless models (also called exospheric) (see *Lemaire and Pierrard* [2001] for a recent review) have been developed since the 1960s to describe the escape of particles from planetary or stellar exobases, defined as the transition region where the mean free path of the particles becomes larger than their density scale height and where the collisions between the particles can be neglected in first approximation. Owing to the assumed lack of collisions above the exobase, no particles are backscattered in the downward loss cone unless via wave-particle interactions. This additional scattering mechanism is ignored here, since at this stage it is difficult to determine the power spectrum of the different waves in the corona and interplanetary medium. In exospheric kinetic models, the VDFs of the particles are truncated due to the absence of thermal solar wind particles coming in from the interplanetary space. Only ballistic, trapped, and escaping particles are considered to contribute to the electron and ion densities, bulk speed, kinetic pressure, etc.

[10] Exospheric models based on Kappa VDF were developed by *Pierrard and Lemaire* [1996]. They have been applied to determine distributions of the solar wind electrons and protons by *Maksimovic et al.* [1997a]. These authors showed that suprathermal tails in electron VDF at the exobase (simulated by low κ_e values) increase the electrostatic potential difference between the exobase altitude and infinity. This larger electric potential difference is necessary to warrant the equality of the proton and electron escape fluxes, i.e., to cancel the net electric current density out of the Sun. As a consequence of this larger electric potential difference, the particles of the corona are accelerated to higher velocities without requiring additional heating processes, as explained by *Meyer-Vernet* [2001].

[11] The first kappa exospheric model of *Pierrard and Lemaire* [1996] for a pure $p^+ - e^-$ solar wind was developed for a total potential energy that is a monotonic increasing function of the radial distance for the electrons and a monotonic decreasing function for the protons. The radial distance of the exobase was 6.6 Rs in their model as in the older exospheric models of *Lemaire and Scherer* [1971, 1973] developed for the low-latitude equatorial solar wind. However, in the coronal holes the plasma density is smaller than at equatorial latitudes. As a consequence, the exobase is located below the altitude where the total potential energy $q(r)$ (defined in equation (23)) of the protons and of the heavy ions have a maximum. The total potential energy of these ions is increasing first with the radial distance; the outward electric force acting on the ions is smaller than the gravitational force so that the net force attracts the positive ions toward the Sun. This situation reverses at larger radial distances where the total force acting on the ions becomes repulsive beyond the radial distance r_m where the potential energy $q(r)$ has its maximum value $q_m(r_m)$.

[12] *Lamy et al.* [2003] have determined the expressions of the moments of a Maxwellian VDF for the case of an exospheric model with a maximum of $q(r)$ at a given distance r_m. In the present paper, we develop a similar exospheric model with a nonmonotonic potential energy but for a Kappa velocity distribution function (see Appendix A).

[13] The model is based on Lorentzian VDFs for the heavy ions of the solar wind since their velocity distribution functions at 1 AU are non-Maxwellian according to the observations of *Collier et al.* [1996]. Moreover, non-Maxwellian distributions with enhanced suprathermal tails tend to increase the temperature of the particles in the corona [*Pierrard and Lamy*, 2003]. The Maxwellian VDF corresponds to a particular case of our Kappa model: when the value of κ tends to infinity, the expressions of the moments for the Kappa function given in Appendix A below and above r_m tend to the expressions derived for the Maxwellian VDF. These expressions have been deduced from the general equations introduced by *Liemohn and Khazanov* [1998] by taking appropriate limiting values given in Table 1. Since some misprints appeared in the paper of Liemohn and Khazanov, the corrected expressions are given in Appendix A using their notations. With these general

Table 1. Limits Corresponding to Integration Regions for the Different Classes of Particles Used in Equations (22), (25), (26), and (27) of *Liemohn and Khazanov* [1998][a]

	r_α	B/B_α	$(\mu_1 B)/(k\tau)$	$\mu_2 B/(k\tau)$	Sign
Ballistic below r_m	r	1	0	$q\eta/(1-\eta)$	+
	r_0	η	$q\eta/(1-\eta)$	$q_m\,\eta/(1-a)$	+
	r_m	μ	0	$q_m\,\eta/(1-a)$	−
Trapped below r_m	r	1	$q\eta/(1-\eta)$	$(q_m-q)\mu/(1-\mu)$	+
	r_0	η	$q\eta/(1-\eta)$	$q_m\,\eta/(1-a)$	−
	r_m	μ	$q_m\,\eta/(1-a)$	$(q_m-q)\mu/(1-\mu)$	−
Escaping below r_m	r_m	μ	0	$q_m\,\eta/(1-a)$	+
	r_0	η	$q_m\,\eta/(1-a)$	∞	+
Escaping beyond r_m	r_m	μ	0	$q_m\,\eta/(1-a)$	+
	r_0	η	$q_m\,\eta/(1-a)$	∞	+

[a]Beyond r_m, only escaping particles are considered in our exospheric model. Below r_m, ballistic and trapped particles have to be added. The moments of ballistic and trapped particles have to be multiplied by two to take into account the upward and the downward component.

expressions for the moments of the VDF, we can calculate the number density, bulk velocity, parallel and perpendicular temperatures of any heavy ion species, for any value of κ. For simplicity, in applications discussed below, we assumed the same value of κ for all the heavy ions. Of course, this assumption can easily be relaxed since there is no obvious reason why κ should be the same.

3. Exospheric Model of the Minor Ions

3.1. Electrostatic Potential Distribution

[14] The electrostatic potential distribution between the exobase and 1 AU is first determined as in the exospheric model described by *Lamy et al.* [2003] assuming that electrons and protons are the dominant species. The number density of the heavier ions is so small compared to the proton density that they do not modify significantly the electrostatic potential determined by the quasi-neutrality equation [*Pierrard and Lamy*, 2003]. It is only when the concentration of helium ions is larger than 10% of that of the protons that He^{2+} do slightly increase the electrostatic potential difference, but this effect is usually negligible compared with the effect of the parameter κ_e and will therefore be ignored hereafter.

[15] Although an extended transition region between the collision-dominated and the collisionless region would be more realistic [*Pierrard et al.*, 2001b], we consider here that the exobase is a sharp cut transition region, just like in the previous exospheric models. We choose the exobase at a radial distance of 2 Rs since coronographic observations of anisotropic ion velocity distributions indicate that there is a sharp increase of the expansion velocity around r = 1.8–2.1 Rs [*Cranmer et al.*, 1999]. This rather confined coronal region corresponds to the location where the characteristic collisional isotropization time begins to exceed the local coronal expansion times for the various ion species.

[16] We assume also that the electron VDF has a significantly enhanced suprathermal tail ($\kappa_e = 2.5$) so that a large electrostatic potential difference of 2750 V is created between the exobase and infinity. The following exobase conditions are considered: $n_{H^+}(r_0) = 2.8 \times 10^{11}$ m^{-3} and $T_e(r_0) = T_p(r_0) = 10^6$ K at the exobase level of $r_0 = 2$ Rs. The electrostatic potential obtained in this case is shown in Figure 1a. It decreases smoothly from 2750 V at the exobase to 0 V at infinity. Owing to this large electrostatic potential, the electrons and protons are accelerated to large bulk

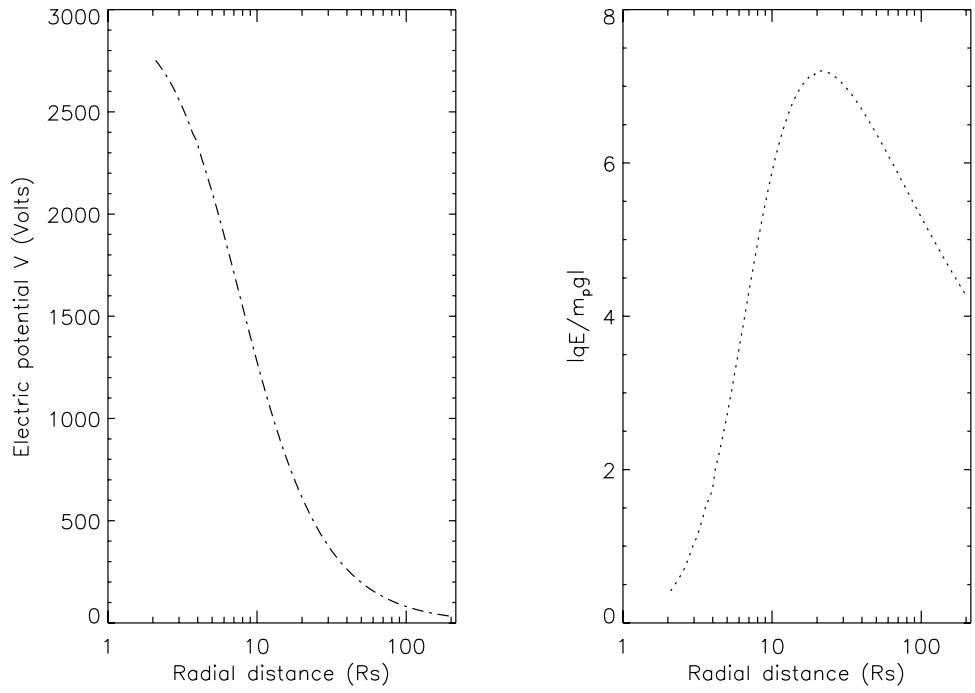

Figure 1. (left) Electrostatic potential obtained from the exobase (2 Rs) to 215 Rs (1 AU) in an exospheric kappa model of solar wind constituted of protons and electrons with $T_e(r_0) = T_p(r_0) = 10^6$ K and $\kappa_e = 2.5$. (right) Ratio of the outward directed electric force (eE) and the inward directed force ($m_{H^+}g$) acting on a proton at different radial distances in the solar wind.

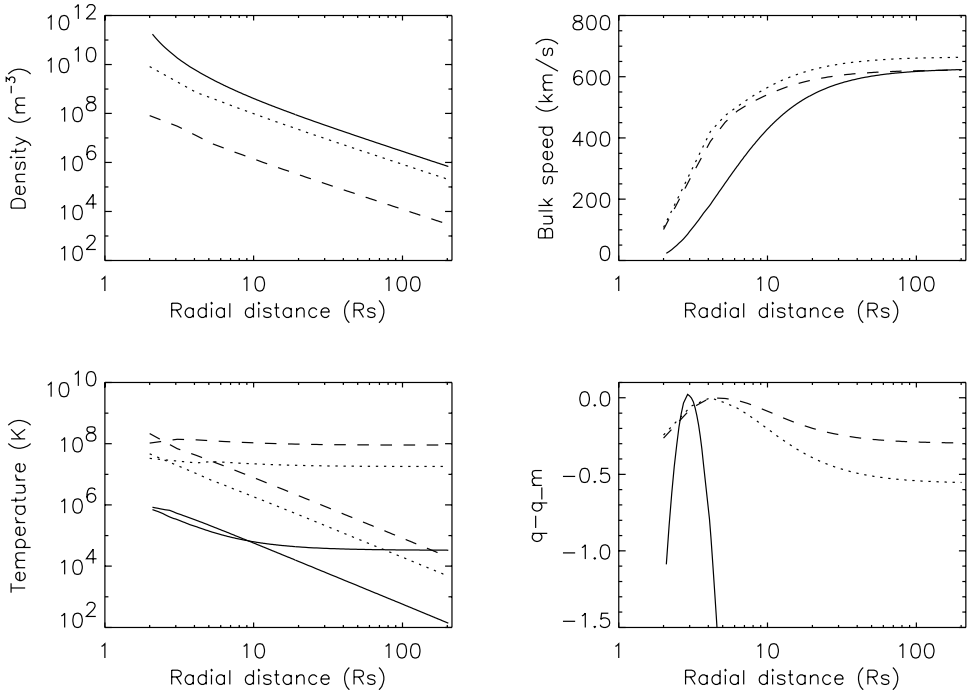

Figure 2. Number density, bulk velocity, parallel (upper lines) and perpendicular temperatures (lower lines), and total normalized potential energy $q - q_m$ as a function of the radial distance in solar radius units (Rs) for protons (solid lines), for He^{2+} (dotted lines), and for O^{6+} ions (dashed lines) obtained with our Lorentzian exospheric model.

velocities (624 km/s at 1 AU in our case study). The bulk velocity of the protons and electrons would even be larger at 1 AU if the exobase level would have been chosen at lower radial distances (<2 Rs) or if κ_e would have been smaller than 2.5.

[17] Figure 1b shows the ratio of the outward directed electric force (eE) and the inward directed gravitational force ($m_{H^+}g$) acting on protons at different radial distances in the solar wind. It can be seen that the outward electric force acting on H^+ exceeds the gravitational force up to a radial distance of 2.8 Rs. Above this radial distance, all protons are accelerated away from the Sun, while below this altitude they are decelerated by the dominant gravitational force. This radial distance corresponds to r_m, the value where the total potential energy of the protons has a maximum.

[18] Since the exobase altitude is located below the distance where $|eE/m_{H^+}g| = 1$, only protons with a large enough kinetic energy can escape out of the potential well and become accelerated to supersonic velocities. They contribute to the evaporation flux of protons as well as to the heat flux out of the Sun, contrary to a large population of ballistic coronal H^+ ions at $r < r_m$ that do not have enough kinetic energy to overcome the total potential barrier.

3.2. Total Normalized Potential Energy of the Ions

[19] Let us now examine the behaviour of the heavy ions in this electrostatic potential distribution. The radial distribution of the mean ion bulk velocity depends on q, the normalized value of the total potential energy (see equation (23)), which has a maximum value q_m at a radial distance r_m which is different for each ion species. The distribution of $q - q_m$ is given as a function of r in Figure 2d for protons (solid line), He^{2+} (dotted line), and O^{6+}(dashed line), which are among the most abundant solar wind ions.

[20] The larger the mass M of the particles, the larger r_m, i.e., the further away from the Sun is the maximum of q. The smaller the charge Z of the ions, the further r_m. Since $M/Z > 1$ (M in amu) for all heavy ions whatever their species and charge states, it results that r_m is always further from the Sun than the corresponding value of r_m for protons for which $M/Z = 1$. For fully ionized ions like for instance oxygen O^{8+}, r_m is the same as for He^{2+} (alpha particles), since both of them have the same M/Z ratio. The values of r_m are given in Table 2 for different ion species in different charge states, including those three illustrated in Figure 2.

[21] Note that the radial distance r_m is independent of the exobase ion temperature T_i and of the value of κ_i; it depends however on the electron temperature T_e and the index κ_e. The value of r_m must be determined with the highest precision to avoid inaccurate velocity profiles of the heavy ions in the exosphere in the vicinity of r_m.

3.3. Acceleration of the Solar Wind Ions

[22] The acceleration of the ions by the outward electric force depends on their charge while their retardation by the gravitational force is controlled by their mass. Owing to their larger mass/charge ratio, He^{2+} ions ($M/Z = 2$) experience a smaller net outward force than the protons. As a consequence of their smaller acceleration, the bulk velocities of He^{2+} ions or heavier ones are expected to be smaller than those of the protons. This statement is correct only if at the exobase, the initial velocities of the protons and heavier ions are the same. Measurements of SOHO indicate however that the heavy ions at 2 Rs have higher temperatures than the protons [*Esser et al.*, 1999]. As a consequence,

Table 2. Exobase Temperatures $T(2Rs)$, Radial Distances r_m Where the Total Potential Energy Has a Maximum, and Predicted Solar Wind Velocity at 215 Rs (1 AU) Obtained With the Lorentzian Exospheric Model With a Very Large Value of $\kappa = 100$[a]

Species	Mass M, amu	Charge Z	M/Z	$T(2Rs)$, 10^6 K	r_m, Rs	$u(\infty)$, km/s
H^+	1.000	1	1.0	1.0	2.796	624
He^+	4.0026	1	4.0	67.0	6.568	567
He^{2+}	4.0026	2	2.0	57.4	4.066	663
C^{4+}	12.011	4	3.0	191.6	5.321	605
C^{5+}	12.011	5	2.4	182.1	4.628	636
N^{4+}	14.007	4	3.5	229.9	5.901	585
O^{5+}	15.999	5	3.2	258.4	5.539	597
O^{6+}	15.999	6	2.7	248.8	4.941	621
O^{7+}	15.999	7	2.3	239.3	4.520	643
Ne^{7+}	20.180	7	2.9	319.3	5.175	611
Mg^{8+}	24.305	8	3.0	388.7	5.352	604
Mg^{9+}	24.305	9	2.7	379.1	4.970	620
Al^{10+}	26.982	10	2.7	420.8	4.970	620
Si^{8+}	28.086	8	3.5	461.1	5.937	584
Si^{9+}	28.086	9	3.1	451.5	5.445	600
Si^{10+}	28.086	10	2.8	441.9	5.089	614
Si^{11+}	28.086	11	2.6	432.4	4.803	628
S^{9+}	32.067	9	3.6	527.7	5.978	582
Ca^{9+}	40.078	9	4.5	681.1	7.204	553
Fe^{9+}	55.845	9	6.2	982.9	10.995	508
Fe^{10+}	55.845	10	5.6	973.3	9.277	524
Fe^{11+}	55.845	11	5.1	963.8	8.212	536
Fe^{12+}	55.845	12	4.7	954.2	7.492	548

[a]The exobase temperatures were calculated with the barometric kappa model of *Pierrard and Lamy* [2003] for $T(1Rs) = 10000$ K and $\kappa = 2.1$ for the different ion species.

their bulk velocities at 1 AU may be larger than that of the protons.

[23] The exobase temperature adopted here for the oxygen ions corresponds to those observed at 2–3 Rs in the corona by UVCS measurements $T_{O^{5+}} = 2.5 \times 10^8$ K [*Esser et al.*, 1999]. *Pierrard and Lamy* [2003] obtained such a high value of $T_{O^{5+}}$ in their hydrostatic model of the low corona (i.e., below the exobase altitude) by postulating that the O^{5+} ion VDF is a Lorentzian with $\kappa = 2.1$. This value of κ is rather small and implies very high suprathermal tails that do not seem easy to maintain in the low corona where Coulomb collisions are important. Therefore they postulate the existence of a physical mechanism that produces continuously suprathermal particles at the base of the solar corona. The origin of this mechanism is not identified, but different processes have been proposed and can explain the predominance of VDFs with suprathermal tails in many space plasmas [*Collier*, 1993; *Treumann*, 1999]. Since the Coulomb collision cross section decreases very fast with the energy, the VDF of the suprathermal particles tend to become Maxwellian over longer time scales than thermal ones. This effect certainly contributes to favor the existence of VDFs with suprathermal tails [*Scudder*, 1992a, 1992b].

[24] Since only a few measurements of minor ion temperatures are available at 2 Rs, we tentatively postulate that the same value of kappa index can be applied to the VDF of all other minor ions. This assumption enables us to predict their temperatures at 2 Rs. It can easily be released in future studies when more experimental observations of coronal ion temperatures will become available. The ion temperatures so determined are found to be more than proportional to the mass of the particles, with slight deviations associated with their charges. The predicted exobase ion temperatures are given in Table 2, e.g., the temperature for He^{2+} is $T_{He^{2+}} = 5.7 \times 10^7$ K at 2 Rs. Owing to the lack of observation from UVCS for all the ions species listed in this table, this procedure has been adopted to determine the temperature of the ions at the exobase level.

[25] With values of κ_i larger than 2.1, the exobase temperatures would have been smaller than in Table 2. However, note that besides or in addition to the velocity filtration effect, there might be other physical processes that can contribute to increase the ion temperatures in the corona. Of course, any other temperature value can be used as boundary condition at the exobase in our exospheric model.

[26] The temperature chosen at the exobase for each ion species is a crucial factor for their bulk velocities at 1 AU. When the exobase temperature is enhanced, the flux of ions that can overrun the potential barrier is enhanced and their bulk velocity becomes then of the order or even larger than that of the protons. The radial distributions of bulk velocities of the protons (solid line), alpha particles (dotted line) and O^{6+} ions (dashed line) are illustrated on Figure 2b. Note that according to our model, the bulk velocity of the heavy ions exceeds already that of the protons at low altitudes in the corona. The rather steep acceleration of heavy ions predicted by our model at low radial distances is in satisfactory agreement with SOHO observations [*Cranmer et al.*, 1999].

[27] The bulk velocities predicted at large radial distance (215 Rs) by our Lorentzian exospheric model are listed in Table 2. It can be seen that some of the heavy ions are accelerated up to velocities in excess to that of the protons. This is especially the case for He^{2+} and the ions with the highest electric charge. On the contrary, very heavy ions like iron are not easily accelerated to velocities larger than that of the protons or helium in this collisionless exospheric model. This happens to be in good agreement with observations indicating that iron ions have a smaller bulk speed than helium ions [*Schmid et al.*, 1987].

[28] To reach still higher bulk velocities for the ions as currently observed in the high-speed solar wind, it would be necessary to start with larger ion temperatures at the exobase or to have a larger electrostatic potential difference between the exobase and infinity. This could be obtained for instance by lowering the altitude of the exobase, e.g., $r_0 = 1.1$ Rs [*Zouganelis et al.*, 2003]. In this case, the protons (and electrons) would also be accelerated to higher bulk velocities by the electrostatic potential difference. It should be pointed out that very high ion temperatures are already reached at 1.1 Rs with the velocity filtration effect due to the sharp temperature gradient obtained between 1 and 1.1 Rs [*Pierrard and Lamy*, 2003].

3.4. Number Densities

[29] At the exobase, located at 2 Rs, the number densities of the most abundant heavy ions are chosen to be $n_{He^{2+}} = 10^{10}$ m^{-3} and $n_{O^{6+}} = 10^8$ m^{-3}. These values correspond to photospheric proportions n_{He}/n_H and n_O/n_H [*Grevesse and Sauval*, 1998]. Most recent spectroscopic and solar wind measurements indicate that the relative chemical abundances above polar coronal holes are of the same order as in the photosphere, while above equatorial regions, elements with low-FIP (first ionization potential) are enhanced by a factor of 4 [*Feldman*, 1998].

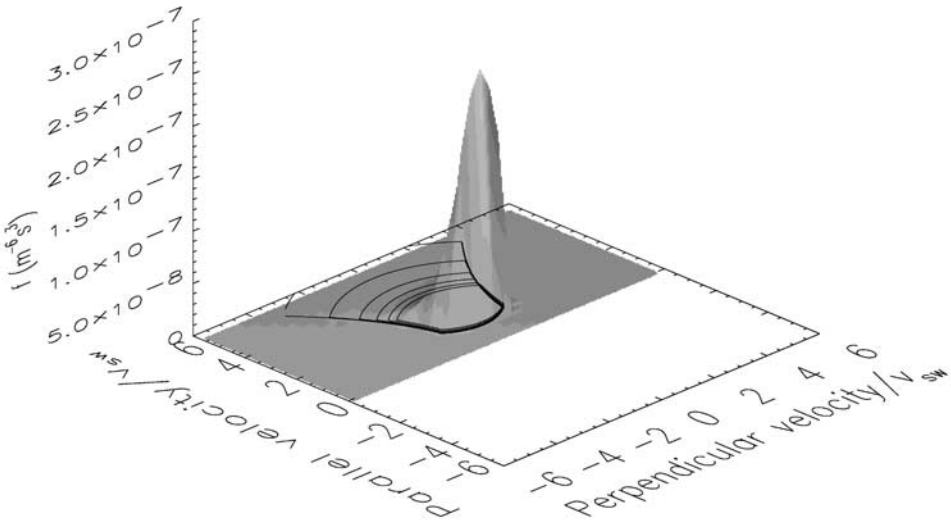

Figure 3. Typical VDF obtained at 1 AU for the minor ion He^{2+} in the exospheric model. The parallel and perpendicular velocities are divided by the solar wind velocity V_{SW}.

[30] In our exospheric model, the number density of the lighter ions decreases a little bit faster with radial distance than that of the heavier particles. In the model, the ratio $n_{He^{2+}}/n_{H^+}$ is larger at 1 AU than at 2 Rs. Nevertheless, the coronal relative abundances of the heavy ions are almost conserved at large radial distances in the solar wind. This is shown in Figure 2a, where all three density profiles are almost parallel to each other, at least when the same value of κ is chosen for the different ion species.

[31] In our exospheric model, the value chosen for the number density of the heavy ions at r_0 is just a normalization factor; changing the value of the exobase density n_0 does not affect either the bulk velocity or the temperature profiles of the heavy ions. If we had chosen larger number densities at the exobase for these heavy ions, their exospheric number density profiles would just have been shifted up or down by a constant factor in Figure 2a.

3.5. Temperatures

[32] Figure 2c illustrates the radial distributions of the parallel temperatures (upper lines at 1 AU) and perpendicular temperatures (lower lines at 1 AU) of the protons, He^{2+} and O^{6+} ions. An interesting characteristic feature of the exospheric Lorentzian model is that the temperature of the minor ions is more than proportional to their mass. This property has been observed in the high-speed solar wind. According to the velocity filtration model of *Pierrard and Lamy* [2003] used to determine the average temperature of the heavy ions in the corona below the exobase, the dispersion of the ion VDF is quasi-proportional to their mass. This mass dependence is slightly enhanced at large radial distances according to our exospheric model. Therefore the ion temperature, which is a measure of the dispersion of the VDF, is larger for heavier ions at 1 AU than for the protons.

[33] Owing to the absence of incoming particles in exospheric models, the perpendicular temperature of the ions is a little bit larger than their parallel temperature at the exobase and immediately above. The temperature anisotropy $T_\parallel/T_\perp$ of the protons reaches 0.4 and remains smaller than 1 up to 9 Rs (see Figure 2c). For the heavier ions, small temperature anisotropies $T_\perp > T_\parallel$ are obtained in a narrow region of the exosphere just above the exobase. At large radial distance, $T_\perp$ decreases rapidly as r^{-2} or $B(r)$ owing to the conservation of the magnetic moment of the particles: $mv_\perp^2/2 \sim B \sim T_\perp$. The parallel temperature is almost independent of r when the magnetic field lines are assumed to be radial and $B \sim r^{-2}$ (no rotation). As a consequence, very large ion temperature anisotropies are obtained at large radial distances compared to the observations and the truncated ion VDFs assumed in the exospheric model are rather different from those deduced from WIND and ULYSSES observations [*Collier et al.*, 1996; *Wimmer-Schweingruber et al.*, 1998]. A typical ion VDF obtained with the exospheric model (here for He^{2+} at 1 AU) is illustrated in three dimensions on Figure 3. Similar truncated VDFs are also assumed for the solar wind protons [*Lemaire and Pierrard*, 2003].

[34] These anisotropies are well-known limitations of all collisionless solar wind models and are a consequence of neglecting Coulomb collisions and wave-particle interactions above the exobase. It was pointed out already by *Lemaire and Scherer* [1971] in their first exospheric solar wind model. Large temperature anisotropies, resulting from the magnetic mirroring force and momentum conservation, are also obtained at 1 AU in other types of solar wind models, for instance in hydrodynamic multifluid models [*Allen and Li*, 2003] or in kinetic models including wave-particle interactions [*Tam and Chang*, 1999]. Different authors have shown that they can be significantly reduced by introducing even a small number of Coulomb collisions per AU [*Griffel and Davis*, 1969; *Lemaire and Scherer*, 1971, 1973; *Phillips and Gosling*, 1990]. Since the Coulomb collision time t_{eq} for energy equipartition between electrons and protons is about 43 times larger than the characteristic time for proton momentum transfer $(t_D)_p$ (i.e., pitch angle scattering of protons), these rare particle-particle interactions constitute an appropriate physical mechanism for reducing the ion temperature anisotropy without chang-

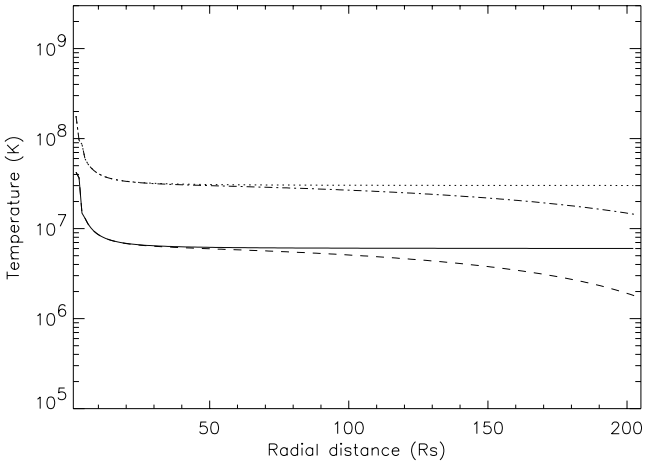

Figure 4. Pitch angle averaged temperatures of He^{2+} obtained for a radial magnetic field (solid line) and for a spiral magnetic field (dashed line) at 70 degrees of latitude. This mean temperature decreases with the radial distance in the case of spiral magnetic field lines. The dotted and dashed-dotted lines correspond to the mean temperature profiles for O^{6+}, respectively, in a radial magnetic field and in a spiral magnetic field distribution.

ing the pitch angle averaged temperature of the protons $\langle T \rangle = (T_{\|} + 2T_{\perp})/3$ at 1 AU. The same argument can be invoked to reduce the ratio of $T_{\|}/T_{\perp}$ for the heavier ions. Small-scale interplanetary magnetic field irregularities and Alfvén waves or plasma instabilities are also possible mechanisms for the isotropization of the ion VDFs in the solar wind. Locally generated waves may lead to perpendicular heating and therefore reduce the temperature anisotropies. These effects that are not included in exospheric models are difficult to evaluate as long as one has not measured the radial and spectral distributions of these waves in the exosphere of the Sun.

[35] It was found also by *Pierrard et al.* [2001a] that a spiral geometry for the interplanetary magnetic field obtained in a rotating ion-exosphere produces adiabatic cooling of the proton parallel temperature, without changing the radial distribution of their number density, bulk velocity, and perpendicular temperature. As a matter of consequence, $T_{\|}/T_{\perp}$ is reduced when the angular velocity of the ion exosphere is enhanced. The same argument and results can be extended for the case of all positive solar wind ions, although such a reduction of $T_{\|}/T_{\perp}$ is too small to explain the actual values reported at 1 AU. For spiral B-field lines, the parallel temperature decreases with the radial distance so that the pitch angle averaged temperatures are lower at 1 AU than in the case of a radial magnetic field. The difference in the omnidirectional temperature is illustrated in Figure 4 for He^{2+} (lower lines) and O^{6+} (upper lines) at a latitude of 70 degrees typical of a coronal hole. The dashed and dotted-dashed lines represent the radial distribution of $\langle T \rangle$ for a corotating ion exosphere, while the solid and dotted ones correspond to a nonrotating exosphere. As a matter of consequence, the ion temperatures at 1 AU are in better agreement with the observations when the corotation of the ion exosphere is taken into account. Indeed, the He^{2+} temperature is observed to be around 1.4×10^6 K at 1 AU in the fast solar wind [*Schwenn*, 1990]. The same observations indicate that $T_{\|}$ is greater than $T_{\perp}$ by about 10 to 30% in the highest speed flows [*Cranmer*, 2002].

[36] The UVCS/SOHO spectrometer can determine temperatures parallel and perpendicular to the assumed radial magnetic field for some coronal ions. Doppler shift observations and Doppler dimming techniques are used for this purpose. The emission lines of hydrogen atoms tend to indicate that the VDFs of these particles have a weak temperature anisotropy at the base of the corona. Similar spectrometric observations indicate that the oxygen ions are characterized by very large temperature anisotropies with $T_{\perp} \gg T_{\|}$ between 2.5 Rs and 3.5 Rs [*Esser et al.*, 1999]. A bi-Lorentzian VDF should better be used to simulate such high coronal anisotropies and should be implemented in future exospheric model. However, the temperature anisotropies of other ion species are not yet known in the corona. Moreover, the value of the temperature anisotropy of O^{5+} is not known unambiguously, since the interpretation of coronographic spectrometer observations remains problematic, especially to separate $T_{\|}$ and $T_{\perp}$ due to line-of-sight effects. Special assumptions are used to determine the ion VDFs from the profiles of emission lines in the region where they are formed. One of these assumptions is that the VDF of the ions is Maxwellian. Of course, if it happens that the VDF would be non-Maxwellian, the inversion process currently used to derive coronal temperatures from line width, should be readdressed. *Scudder* [1992a] has derived the observable consequences of nonthermal distributions in the coronal line emission and absorption profiles.

4. Influence of κ_i Index

[37] The value of the exobase temperature T_0 of the ions is the crucial parameter controlling their bulk velocity at large radial distances. However, for a given value of T_0, the index κ_i has also some influence in exospheric models. Figure 5 illustrates the bulk velocities of He^{2+} and O^{6+} obtained at 1 AU for two different values: $\kappa_i = 2.1$ (dotted line) and $\kappa_i \rightarrow \infty$ (Maxwellian case, solid line). The index κ_i of the ion VDFs has a rather limited influence on the distribution of their moments. In particular, Figure 5 illustrates that it only slightly affects their bulk velocity at large radial distance. When κ_i is reduced in the exospheric model, the ion bulk speed at 1 AU is reduced for large exobase temperatures but increased for low temperatures.

[38] The values of $u(\infty)$, the bulk velocities at 215 Rs, given in Table 2, are obtained with the exospheric Lorentzian model with an extremely large value of κ_i, in order to evidence that the acceleration of the ions in the exosphere is not a consequence of the smallness of the index κ_i but of their high exobase temperature. The presence of suprathermal tails in the ion VDFs at the base of the corona is not the cause of their acceleration to high supersonic speed.

5. Influence of κ_e

[39] It is the enhanced population of suprathermal electrons that determines the large electrostatic potential which accelerates the solar wind ions. In our example, we choose $\kappa_e = 2.5$ because such low values are obtained by fitting the electron VDFs observed in the solar wind at 1 AU during

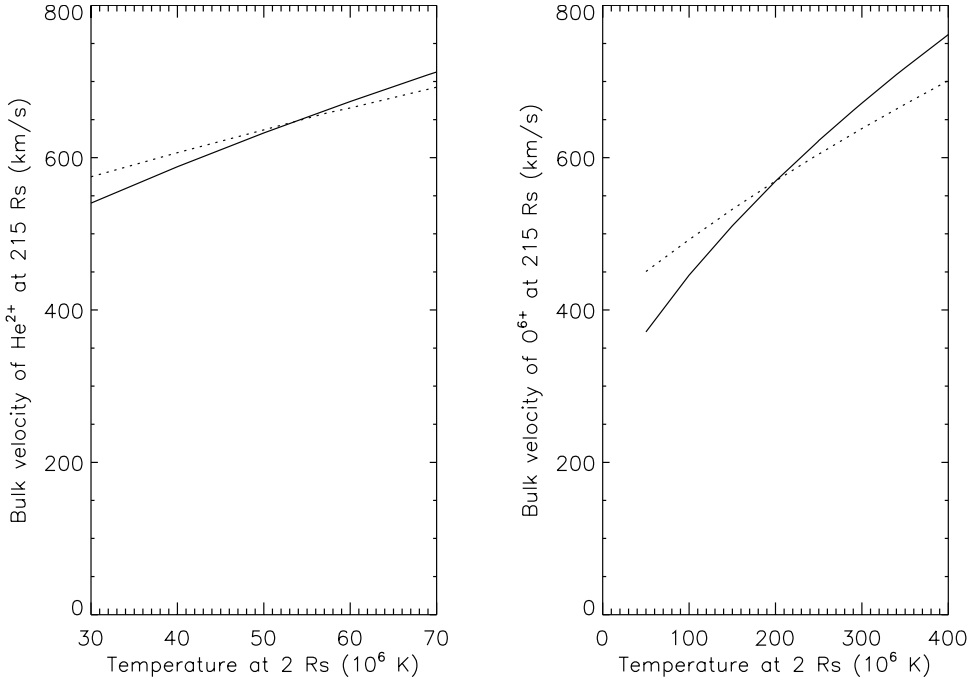

Figure 5. Ion bulk velocity obtained with the Lorentzian exospheric model at 215 Rs (1 AU) as a function of the ion exobase temperature. The solid lines correspond to Maxwellian VDF ($\kappa \rightarrow \infty$), and the dotted lines correspond to a Lorentzian exosphere for which $\kappa_i = 2.1$. The He^{2+} ions are represented in the left panel and the O^{6+} ions in the right panel.

the ULYSSES mission [*Maksimovic et al.*, 1997b]. The index κ of a VDF is independent of the radial distance in the Lorentzian exospheric model so that the index κ_e should be the same at large radial distances in the solar wind as at the exobase. Also, *Esser and Edgar* [2000] showed that the existence of an important population of suprathermal electrons in the corona provide an explanation for some in situ charge states. Nevertheless, other experimental determinations of κ_e by *Ko et al.* [1997] suggest a larger value of $\kappa_e \sim 5$ in the low corona. Of course, with such a larger value of κ_e, the electrostatic potential difference is smaller than 2000 V, and the bulk velocities of the particles are reduced accordingly to values corresponding to the low-latitude quiet solar wind. Keeping the same temperatures at the exobase, the bulk velocity of the protons is then more reduced than that of the ions for which $M/Z > 1$. Note that with an exobase level located below 2 Rs, it would be possible to reach values of $u(\infty)$ as large as those given in Table 2 even with a higher value of κ_e.

6. Discussion and Conclusions

[40] Since collisions are relatively unimportant in the low-density extended coronal holes and interplanetary medium, a kinetic treatment of the corona and the high-speed solar wind is useful. Indeed, in the solar corona, the UVCS observations of SOHO demonstrate that the different ion species exhibit an extreme diversity of temperature ranges. In the solar wind, in situ measurements of the ion velocity dispersions confirm that the solar wind plasma is closer to a collisionless medium than to a classic thermodynamic fluid.

[41] Kinetic models can be used to determine the velocity distribution function of protons and electrons and also of the minor ions in the transition region and throughout the whole exosphere. The minor ions do not contribute significantly to the total particle density of the solar wind, but their study is interesting because they carry the signature of the "heating" and acceleration processes.

[42] In the present paper, we have included the minor ions in the kappa exospheric model of the solar wind. For this reason, the model has been extended to the case when the exobase is located below the altitude of a nonmonotonic potential energy distribution, where the gravitational force is larger than the outward electric force for the ions.

[43] In exospheric models, the electrons and different ion species are handled separately in the gravitational and electric potentials. The collisionless models of the solar wind provide convenient analytic expressions for the moments of the VDF and take into account the role of the internal polarization electric field in the acceleration process of the ions.

[44] We show that for very high ion temperatures in the corona, the ion bulk velocities predicted at 1 AU can become as large as observed in the fast solar wind. The number density and temperature of the different ion species are also calculated with our extended version of the exospheric kappa model. Their distributions are compared with the observations in the solar corona and in the solar wind. The agreement is quite good except for the temperature anisotropies, which remain too large compared with the observations. Additional Coulomb collisions neglected in exospheric models, wave-particle interactions and effects of a spiral magnetic field can reduce the temperature anisotropies.

[45] The solutions of the exospheric modeldepend only on a rather small number of free parameters constrained by coronal observations: the altitude of the exobase, the exobase temperature of the particles, and the κ index charac-

terizing the Lorentzian VDF of the particle species. Their influence on the results has been discussed in the paper.

[46] The exospheric model provides criteria involving the ion temperatures that govern their bulk velocities at large distances of the solar wind. High ion bulk velocities are reached at large radial distances by assuming very high ion temperatures in the corona. Since UVCS temperature measurements are not available for all ion species in the corona, the ion temperatures at the exobase have been calculated in this case study using the velocity filtration model. As a result of the velocity filtration, the coronal temperatures of ions are more than proportional to the mass, with a small correction due to their electric charge [*Pierrard and Lamy*, 2003]. Large bulk speeds are then obtained at 1 AU without assuming extra in situ heating or momentum transfer to the ions by wave-particle interactions.

[47] The high ion temperatures can be attributed to other physical processes and especially to the dissipation of high-frequency waves that are resonant with ion cyclotron motions. This mechanism can lead to large temperature anisotropies with $T_\perp \gg T_\parallel$ for the solar wind ions in the inner corona and may also reproduce many features observed in the solar wind [*Cranmer*, 2000; *Isenberg*, 2001]. However, the specific mechanisms generating the required waves are currently unclear [*Cranmer*, 2002]. Moreover, ion-cyclotron waves (with frequencies between 10 and 10^4 Hz) have not yet been observed in the solar wind or in the corona, and if they exist, their fluctuating power must be much smaller than that of low-frequency Alfvén waves. Note that some minor ions have cyclotron frequencies considerably lower than that of the protons. Their ion cyclotron motions are therefore more compatible with waves of lower frequency, such as the Alfven waves.

[48] Fast shocks have also been suggested to accelerate the solar wind ions [*Lee*, 2001], but there is no evidence that shocks of the required strength are numerous enough in the corona to heat and accelerate most of the ions to the observed level. In the near future, more detailed observations of the ions in the solar corona should allow us to determine more definitely the relative importance of these different mechanisms.

[49] Of course, more detailed kinetic models taking into account Coulomb collisions as well as possibly wave-particle interactions should be developed. Some kinetic models including Coulomb collisions [*Lie-Svendsen et al.*, 1997; *Pierrard et al.*, 1999, 2001b] and wave-particle interactions [*Tam and Chang*, 1999; *Vocks and Marsch*, 2001] have been proposed, as well as multifluid hydrodynamical models including heavy ions [*Bodmer and Bochsler*, 2000; *Allen and Li*, 2003]. All these models take into account dissipative irreversible mechanisms that possibly contribute to the radial distribution of the solar wind plasma. The present work shows the importance of high exobase ion temperatures and the influence of the electric field in the acceleration mechanism of the solar wind ions.

Appendix A: Moments of a Lorentzian Velocity Distribution Function

[50] Our exospheric Kappa model is based on the analytical formulae in equations (25) to (31) derived by *Liemohn and Khazanov* [1998]. Note, however, the following corrections to their equations (27), (28), and (30):

$$P^L_{\perp,gen} = P^L_{//,gen} + \frac{n_0\tau}{2}\kappa\xi^1_\kappa \left\{ \frac{B}{B_\alpha} \frac{\left(1-\frac{B}{B_\alpha}\right)^{\kappa-1}}{\zeta_0^{\kappa-3/2}} \cdot \left[H_1(z_1^*, z_2^*) \frac{\Pi - \Pi_\alpha}{\kappa\tau(1-B/B_\alpha)} + H_2(z_1^*, z_2^*) \right] + \frac{\mu_1 B}{\tau\kappa} \frac{H_1(0,z_1)}{\zeta_1^{\kappa-3/2}} - \frac{\mu_2 B}{\tau\kappa} \frac{H_1(0,z_2)}{\zeta_2^{\kappa-3/2}} \right\} \tag{A1}$$

$$\epsilon^L_{\parallel,gen} = (\Pi_\alpha - \Pi)\Phi^L_{gen} + \frac{n_0}{2}\left(\frac{2\tau}{\pi m}\right)^{1/2} \frac{B}{B_\alpha} \frac{\xi^0_\kappa}{\kappa^{1/2}(\kappa-1)} \cdot \left(\mu_1 B_\alpha \left(\zeta_1^\alpha\right)^{-(\kappa-1)} - \mu_2 B_\alpha \left(\zeta_2^\alpha\right)^{-(\kappa-1)} + \frac{2\kappa\tau}{\kappa-2}\left[\left(\zeta_1^\alpha\right)^{-(\kappa-2)} - \left(\zeta_2^\alpha\right)^{-(\kappa-2)} \right] \right) \tag{A2}$$

$$z^*_{1,2} = \frac{\xi_0}{\left(1-\frac{B}{B_\alpha}\right)\left(1+\frac{\mu_{1,2}B_\alpha + \pi_\alpha - \pi_0}{\kappa\tau}\right)}. \tag{A3}$$

[51] For completeness, it is also necessary to add a test on $B/B\alpha$ in equations (25), (26), and (27) of *Liemohn and Khazanov* [1998]; indeed, if $B/B\alpha > 1$, then one should use

$$n^L_{gen} = \frac{n_0}{2}\xi^1_\kappa \left\{ \frac{\left(\frac{B}{B_\alpha}-1\right)^\kappa}{-\zeta_0^{\kappa-1/2}} H_1'(z_1^*, z_2^*) + \frac{H_1(0,z_1)}{\zeta_1^{\kappa-1/2}} - \frac{H_1(0,z_2)}{\zeta_2^{\kappa-1/2}} \right\} \tag{A4}$$

$$P^L_{//,gen} = \frac{n_0\tau}{3}\kappa\xi^1_\kappa \left\{ \frac{\left(\frac{B}{B_\alpha}-1\right)^\kappa}{-\zeta_0^{\kappa-3/2}} H_2'(z_1^*, z_2^*) + \frac{H_2(0,z_1)}{\zeta_1^{\kappa-3/2}} - \frac{H_2(0,z_2)}{\zeta_2^{\kappa-3/2}} \right\} \tag{A5}$$

$$P^L_{\perp,gen} = P^L_{//,gen} + \frac{n_0\tau}{2}\kappa\xi^1_\kappa \left\{ \frac{B}{B_\alpha} \frac{\left(\frac{B}{B_\alpha}-1\right)^{\kappa-1}}{-\zeta_0^{\kappa-3/2}} \cdot \left[H_1'(z_1^*, z_2^*) \frac{\Pi - \Pi_\alpha}{\kappa\tau(1-B/B_\alpha)} + H_2'(z_1^*, z_2^*) \right] + \frac{\mu_1 B}{\tau\kappa} \frac{H_1(0,z_1)}{\zeta_1^{\kappa-3/2}} - \frac{\mu_2 B}{\tau\kappa} \frac{H_1(0,z_2)}{\zeta_2^{\kappa-3/2}} \right\} \tag{A6}$$

with

$$H_1'(u_1,u_2) = \int_{u_1}^{u_2} t^{\kappa-3/2}(t-1)^{1/2} dt \tag{A7}$$

$$H_2'(u_1,u_2) = \int_{u_1}^{u_2} t^{\kappa-5/2}(t-1)^{3/2} dt \tag{A8}$$

with $u_1, u_2 \geq 1$. In the case of the solar wind, $B/B\alpha > 1$ below r_m where $\mu > 1$.

[52] The following definitions are used in this appendix:

$$\frac{B(r)}{B(r_0)} = \eta \tag{A9}$$

$$\frac{B(r)}{B(r_m)} = \mu \tag{A10}$$

$$\frac{B(r_m)}{B(r_0)} = a = \frac{\eta}{\mu} \tag{A11}$$

$$\frac{(\Pi_m - \Pi_0)B}{(B_0 - B_m)k\tau} = \frac{q_m \frac{B}{B_0}}{1 - \frac{B_m}{B_0}} = \frac{q_m \eta}{1 - a} \tag{A12}$$

$$\frac{(\Pi - \Pi_0)B}{(B_0 - B)k\tau} = q\frac{\eta}{(1-\eta)} \tag{A13}$$

$$\frac{(\Pi_m - \Pi)B}{(B - B_m)k\tau} = (q_m - q)\frac{\mu}{(\mu - 1)}. \tag{A14}$$

[53] "Kappa" functions are defined by

$$f = n_0\left(\frac{m}{2kT\pi\kappa}\right)^{3/2}\frac{\Gamma(\kappa+1)}{\Gamma(\kappa-1/2)}\left(1+\frac{v^2}{\kappa w^2}\right)^{-(\kappa+1)}, \tag{A15}$$

where

$$\frac{mw^2}{2} = \frac{2\kappa - 3}{2\kappa}kT \tag{A16}$$

is the average kinetic energy, m is the mass of the particle, k is the Boltzmann constant, n_0 is the number density, $\Gamma(x)$ is the Gamma function, and κ is the index which determines the slope of the energy spectrum for the suprathermal particles. The larger the value of κ, the lesser the excess of suprathermal particles.

A1. Beyond r_m: Escaping Ions

[54] The following formulae apply for the escaping ions beyond r_m.

Density

$$n^e(r) = \frac{n_0}{2}\left[\left(1+\frac{q}{\kappa}\right)^{-\kappa+1/2}\beta_2(z_1) - (1-\eta)^{1/2} \cdot \left(1+\frac{q}{\kappa(1-\eta)}\right)^{-\kappa+1/2}\beta_2(Z_1'^*) + (1-\mu)^{1/2} \cdot \left(1+\frac{q-\mu q_m}{\kappa(1-\mu)}\right)^{-\kappa+1/2}[\beta_2(z_2^*) - \beta_2(z_1^*)]\right] \tag{A17}$$

Flux

$$F^e(r) = \frac{n_0}{2}\sqrt{\frac{2k\tau}{m\pi}}\frac{\Gamma(\kappa+1)}{\Gamma(\kappa-1/2)}\frac{1}{\kappa^{1/2}(\kappa-1)} \cdot \left[\mu\left(1+\frac{q_m}{\kappa}\right)^{-\kappa+1} + (\eta-\mu)\left(1+\frac{q_m}{\kappa(1-a)}\right)^{-\kappa+1}\right] \tag{A18}$$

Parallel pressure

$$P_\parallel^e(r) = \frac{n_0 k\tau}{3}\frac{A_k}{A_k'}\kappa\left[\left(1+\frac{q}{\kappa}\right)^{-\kappa+3/2} \cdot \beta_4(z_1) - (1-\eta)^{3/2}\left(1+\frac{q}{\kappa(1-\eta)}\right)^{-\kappa+3/2} \cdot \beta_4(Z_1'^*) + (1-\mu)^{3/2}\left(1+\frac{q-\mu q_m}{\kappa(1-\mu)}\right)^{-\kappa+3/2} \cdot [\beta_4(z_2^*) - \beta_4(z_1^*)]\right] \tag{A19}$$

Perpendicular pressure

$$\begin{aligned} P_\perp^e(r) &= P_\parallel^e + \frac{n_0 k\tau}{2}\frac{A_k}{A_k'}\kappa\left[\eta(1-\eta)^{1/2}\left(1+\frac{q}{\kappa(1-\eta)}\right)^{-\kappa+3/2} \cdot \left(-\beta_4(Z_1'^*) - \frac{A_k'}{A_k}\beta_2(Z_1'^*)\frac{q}{\kappa(1-\eta)}\right) + \mu(1-\mu)^{1/2}\left(1+\frac{q-\mu q_m}{\kappa(1-\mu)}\right)^{-\kappa+3/2} \cdot \left(\beta_4(z_2^*) - \beta_4(z_1^*) + \frac{A_k'}{A_k} \cdot (\beta_2(z_2^*) - \beta_2(z_1^*))\frac{q-q_m}{\kappa(1-\mu)}\right)\right] \\ &= \frac{n_0 k\tau}{3}\frac{A_k}{A_k'}\kappa\left[\left(1+\frac{q}{\kappa}\right)^{-\kappa+3/2}\beta_4(z_1) - (1-\eta)^{1/2}\left(1+\frac{q}{\kappa(1-\eta)}\right)^{-\kappa+3/2} \cdot \left(\beta_4(Z_1'^*)\left(1+\frac{\eta}{2}\right) + \frac{3}{2}\frac{A_k'}{A_k}\beta_2(Z_1'^*)\frac{q\eta}{\kappa(1-\eta)}\right) + (1-\mu)^{1/2}\left(1+\frac{q-\mu q_m}{\kappa(1-\mu)}\right)^{-\kappa+3/2} \cdot \left((\beta_4(z_2^*) - \beta_4(z_1^*))\left(1+\frac{\mu}{2}\right) + \frac{3}{2}\frac{A_k'}{A_k}(\beta_2(z_2^*) - \beta_2(z_1^*))\frac{(q-q_m)\mu}{\kappa(1-\mu)}\right)\right] \end{aligned} \tag{A20}$$

Heat flux

$$\epsilon^e(r) = \frac{n_0}{2}\sqrt{\frac{2k\tau}{\pi m}}k\tau\frac{\Gamma(\kappa+1)}{\Gamma(\kappa-1/2)}\frac{1}{\sqrt{\kappa}(\kappa-1)} \cdot \left[\left(1+\frac{q_m}{\kappa}\right)^{-\kappa+1}\left[\mu\left(q_m - q + \frac{2\kappa}{\kappa-2}\left(1+\frac{q_m}{\kappa}\right)\right)\right] + \left(1+\frac{q_m}{(1-a)\kappa}\right)^{-\kappa+1} \cdot \left[(\eta-\mu)\left(\frac{2\kappa}{\kappa-2}\left(1+\frac{q_m}{\kappa(1-a)}\right) - q\right) - \mu q_m\right]\right] \tag{A21}$$

with

$$\tau = T\frac{\kappa - 3/2}{\kappa} \tag{A22}$$

$$q = \frac{m\phi_g(r) + ZeV(r) - m\phi_g(r_0) - ZeV(r_0)}{k\tau} \tag{A23}$$

$$q_m = \frac{m\phi_g(r_m) + ZeV(r_m) - m\phi_g(r_0) - ZeV(r_0)}{k\tau} \tag{A24}$$

$$A_k = \frac{\Gamma(\kappa+1)}{\Gamma(\kappa-1/2)\Gamma(3/2)} \tag{A25}$$

$$A'_k = \frac{\Gamma(\kappa+1)}{\Gamma(\kappa-3/2)\Gamma(5/2)} \tag{A26}$$

$$\beta_2(x) = \int_0^x A_k t^{\kappa-3/2}(1-t)^{1/2}dt \tag{A27}$$

$$\beta_4(x) = \int_0^x A'_k t^{\kappa-5/2}(1-t)^{3/2}dt \tag{A28}$$

$$z_1 = \frac{\kappa+q}{\kappa+q_m} \tag{A29}$$

$$z_1^* = \frac{\kappa(1-\mu)+q-\mu q_m}{(\kappa+q_m)(1-\mu)} \tag{A30}$$

$$z_2^* = \frac{\kappa(1-\mu)+q-\mu q_m}{(\kappa+q_m/(1-a))(1-\mu)} \tag{A31}$$

$$Z_1'^* = \frac{\kappa(1-\eta)+q}{(\kappa+q_m/(1-a))(1-\eta)} \tag{A32}$$

$$z_2 = Z'_1 \tag{A33}$$

$$Z_2'^* = 0 \tag{A34}$$

A2. Below r_m

[55] The following formulae apply for the ions below r_m.

A2.1. Ballistic Ions

[56] Density

$$n^b(r) = n_0\left[\left(1+\frac{q}{\kappa}\right)^{-\kappa+1/2}(1-\beta_2(z_1)) - (1-\eta)^{1/2}\left(1+\frac{q}{\kappa(1-\eta)}\right)^{-\kappa+1/2}\cdot\left(1-\beta_2\left(Z_1'^*\right)\right) + (\mu-1)^{1/2}\cdot\left(1+\frac{q-\mu q_m}{\kappa(1-\mu)}\right)^{-\kappa+1/2}\beta'_2(z_1^*,z_2^*)\right] \tag{A35}$$

[57] Flux

$$F^b(r) = 0 \tag{A36}$$

Parallel pressure

$$P_\parallel^b(r) = \frac{2n_0k\tau}{3}\frac{A_k}{A'_k}\kappa\left[\left(1+\frac{q}{\kappa}\right)^{-\kappa+3/2}\cdot(1-\beta_4(z_1)) - (1-\eta)^{3/2}\cdot\left(1+\frac{q}{\kappa(1-\eta)}\right)^{-\kappa+3/2}\left(1-\beta_4\left(Z_1'^*\right)\right) + (\mu-1)^{3/2}\left(1+\frac{q-\mu q_m}{\kappa(1-\mu)}\right)^{-\kappa+3/2}\beta_4(z_1^*,z_2^*)\right] \tag{A37}$$

Perpendicular pressure

$$P_\perp^b(r) = P_\parallel^b - n_0k\tau\frac{A_k}{A'_k}\kappa\left[\eta(1-\eta)^{1/2}\left(1+\frac{q}{\kappa(1-\eta)}\right)^{-\kappa+3/2}\cdot\left(1-\beta_4\left(Z_1'^*\right)+\frac{A'_k}{A_k}\left(1-\beta_2\left(Z_1'^*\right)\right)\frac{q}{\kappa(1-\eta)}\right) - \mu(\mu-1)^{1/2}\left(1+\frac{q-\mu q_m}{\kappa(1-\mu)}\right)^{-\kappa+3/2}\cdot\left(\beta'_4(z_1^*,z_2^*)+\frac{A'_k}{A_k}\beta'_2(z_1^*,z_2^*)\frac{q-q_m}{\kappa(1-\mu)}\right)\right] \tag{A38}$$

Heat flux

$$\epsilon^b(r) = 0 \tag{A39}$$

with

$$\beta'_2(z_1,z_2) = \int_{z_1}^{z_2} A_k t^{\kappa-3/2}(t-1)^{1/2}dt \tag{A40}$$

$$\beta'_4(z_1,z_2) = \int_{z_1}^{z_2} A'_k t^{\kappa-5/2}(t-1)^{3/2}dt \tag{A41}$$

A2.2. Trapped Ions

[58] Density

$$n^t(r) = n_0\left[(1-\eta)^{1/2}\left(1+\frac{q}{\kappa(1-\eta)}\right)^{-\kappa+1/2}\cdot\left(1-\beta_2\left(Z_1'^*\right)\right) - (\mu-1)^{1/2}\cdot\left(1+\frac{q-\mu q_m}{\kappa(1-\mu)}\right)^{-\kappa+1/2}\left[\beta'_2(1,z_2^*)\right]\right] \tag{A42}$$

Flux

$$F^t(r) = 0 \tag{A43}$$

[59] Parallel pressure

$$P_\parallel^t(r) = \frac{2n_0k\tau}{3}\frac{A_k}{A'_k}\kappa\left[(1-\eta)^{3/2}\cdot\left(1+\frac{q}{\kappa(1-\eta)}\right)^{-\kappa+3/2}\left(1-\beta_4\left(Z_1'^*\right)\right) - (\mu-1)^{3/2}\left(1+\frac{q-\mu q_m}{\kappa(1-\mu)}\right)^{-\kappa+3/2}\left[\beta'_4(1,z_2^*)\right]\right] \tag{A44}$$

[60] Perpendicular pressure

$$P_\perp^t(r) = P_\parallel^t + n_0k\tau\frac{A_k}{A'_k}\kappa\left[\eta(1-\eta)^{1/2}\cdot\left(1+\frac{q}{\kappa(1-\eta)}\right)^{-\kappa+3/2}\cdot\left(1-\beta_4\left(Z_1'^*\right)+\frac{A'_k}{A_k}\left(1-\beta_2\left(Z_1'^*\right)\right)\frac{q}{\kappa(1-\eta)}\right) - \mu(\mu-1)^{1/2}\left(1+\frac{q-\mu q_m}{\kappa(1-\mu)}\right)^{-\kappa+3/2}\cdot\left(\beta'_4(1,z_2^*)+\frac{A'_k}{A_k}\beta'_2(1,z_2^*)\frac{q-q_m}{\kappa(1-\mu)}\right)\right] \tag{A45}$$

[61] Heat flux

$$\epsilon^t(r) = 0 \tag{A46}$$

A.2.3. Escaping Ions

[62] Density

$$n^e(r) = \frac{n_0}{2}\left[\left(1+\frac{q}{\kappa}\right)^{-\kappa+1/2}\beta_2(z_1) - (1-\eta)^{1/2}\left(1+\frac{q}{\kappa(1-\eta)}\right)^{-\kappa+1/2}\beta_2\left(Z_1'^*\right) - (\mu-1)^{1/2}\left(1+\frac{q-\mu q_m}{\kappa(1-\mu)}\right)^{-\kappa+1/2}\cdot\beta'_2(z_1^*,z_2^*)\right] \tag{A47}$$

[63] Flux

$$F^e(r) = \frac{n_0}{2}\sqrt{\frac{2k\tau}{m\pi}}\frac{\Gamma(\kappa+1)}{\Gamma(\kappa-1/2)}\frac{1}{\kappa^{1/2}(\kappa-1)} \cdot \left[\mu\left(1+\frac{q_m}{\kappa}\right)^{-\kappa+1} + (\eta-\mu)\left(1+\frac{q_m}{\kappa(1-a)}\right)^{-\kappa+1}\right] \quad \text{(A48)}$$

[64] Parallel pressure

$$P_\parallel^e(r) = \frac{n_0 k\tau}{3}\frac{A_k}{A_k'}\kappa\left[\left(1+\frac{q}{\kappa}\right)^{-\kappa+3/2}\beta_4(z_1) - (1-\eta)^{3/2}\left(1+\frac{q}{\kappa(1-\eta)}\right)^{-\kappa+3/2}\beta_4(Z_1'^*) - (\mu-1)^{3/2}\left(1+\frac{q-\mu q_m}{\kappa(1-\mu)}\right)^{-\kappa+3/2}\beta_4'(z_1^*, z_2^*)\right] \quad \text{(A49)}$$

[65] Perpendicular pressure

$$P_\perp^e(r) = P_\parallel^e + \frac{n_0 k\tau}{2}\frac{A_k}{A_k'}\kappa\left[\eta(1-\eta)^{1/2}\left(1+\frac{q}{\kappa(1-\eta)}\right)^{-\kappa+3/2} \cdot \left(-\beta_4(Z_1'^*) - \frac{A_k'}{A_k}\beta_2(Z_1'^*)\frac{q}{\kappa(1-\eta)}\right) - \mu(\mu-1)^{1/2}\left(1+\frac{q-\mu q_m}{\kappa(1-\mu)}\right)^{-\kappa+3/2}\left(\beta_4'(z_1'^*, z_2'^*) + \frac{A_k'}{A_k}\beta_2'(z_1^*, z_2^*)\frac{q-q_m}{\kappa(1-\mu)}\right)\right] \quad \text{(A50)}$$

[66] Heat flux

$$\epsilon^e(r) = \frac{n_0}{2}\sqrt{\frac{2k\tau}{\pi m}}k\tau\frac{\Gamma(\kappa+1)}{\Gamma(\kappa-1/2)}\frac{1}{\sqrt{\kappa}(\kappa-1)}\left[\left(1+\frac{q_m}{\kappa}\right)^{-\kappa+1} \cdot \left[\mu\left(q_m - q + \frac{2\kappa}{\kappa-2}\left(1+\frac{q_m}{\kappa}\right)\right)\right] + \left(1+\frac{q_m}{(1-a)\kappa}\right)^{-\kappa+1} \cdot \left[(\eta-\mu)\left(\frac{2\kappa}{\kappa-2}\left(1+\frac{q_m}{\kappa(1-a)}\right) - q\right) - \mu q_m\right]\right] \quad \text{(A51)}$$

In the limit of $\kappa \to \infty$, one recovers the expressions obtained by *Lamy et al.* [2003] for a Maxwellian VDF in a nonmonotonic distribution of the potential energy.

[67] **Acknowledgments.** This work has been performed on the grants MO/35/008 and Action 1 of the Belgian SPP Politique Scientifique Fédérale.

[68] Shadia Rifai Habbal thanks the referees for their assistance in evaluating this paper.

References

Allen, L., and X. Li (2003), A three-fluid, 16 moment gyrotropic bi-Maxwellian fast solar wind: The effect of He^{++}, in *Solar Wind Ten*, edited by M. Velli et al., *AIP Conf. Proc.*, *679*, 339–342.

Bodmer, R., and P. Bochsler (2000), Influence of Coulomb collisions on isotopic and elemental fractionation in the solar wind acceleration process, *J. Geophys. Res.*, *105*, 47–62.

Collier, M. C. (1993), On generating kappa-like distribution functions using velocity space Levy flights, *Geophys. Res. Lett.*, *20*, 1531–1534.

Collier, M. C., D. C. Hamilton, G. Gloeckler, P. Bochsler, and R. B. Sheldon (1996), Neon-20, Oxygen-16, and Helium 4 densities, temperatures, and suprathermal tails in the solar wind determined by WIND/MASS, *Geophys. Res. Lett.*, *23*, 1191–1194.

Cranmer, S. R. (2000), Ion cyclotron wave dissipation in the solar corona: the summed effect of more than 2000 ion species, *Astrophys. J.*, *532*, 1197–1208.

Cranmer, S. R. (2002), Coronal holes and the high-speed solar wind, *Sp. Sci. Rev.*, *101*, 229–294.

Cranmer, S. R., et al. (1999), An empirical model of a polar coronal hole at solar minimum, *Astrophys. J.*, *511*, 481–501.

Dorelli, J. C., and J. D. Scudder (1999), Electron heat flow carried by Kappa distributions in the solar corona, *Geophys. Res. Lett.*, *23*, 3537–3540.

Esser, R., and R. J. Edgar (2000), Reconciling spectroscopic electron temperature measurements in the solar corona with in-situ charge state observations, *Astrophys. J. Lett.*, *532*, L71–74.

Esser, R., S. Fineschi, D. Dobrzycka, S. R. Habbal, R. J. Edgar, J. C. Raymond, J. L. Kohl, and M. Guhathakurta (1999), Plasma properties in coronal holes derived from measurements of minor ion spectral lines and polarized white light intensity, *Astrophys. J.*, *510*, L63–L67.

Feldman, U. (1998), FIP effect in the solar upper atmosphere: spectroscopic results, *Space Sci. Rev.*, *85*, 227–240.

Grevesse, N., and A. J. Sauval (1998), Standard solar composition, *Space Sci. Rev.*, *85*, 161–174.

Griffel, D. H., and L. Davis (1969), The anisotropy of the solar wind, *Planet. Space Sci.*, *17*, 1009–1020.

Isenberg, P. A. (2001), Heating of coronal holes and generation of the solar wind by ion-cyclotron resonance, *Space Sci. Rev.*, *95*, 119–131.

Ko, Y.-K., L. A. Fisk, J. Geiss, G. Gloeckler, and M. Guhathakurta (1997), An empirical study of the electron temperature and heavy ion velocities in the south polar coronal hole, *Sol. Phys.*, *171*, 345–361.

Kohl, J. L., et al. (1997), First results from the SOHO ultraviolet coronograph spectrometer, *Sol. Phys.*, *175*, 613–644.

Lamy, H., V. Pierrard, M. Maksimovic, and J. Lemaire (2003), A kinetic exospheric model of the solar wind with a non monotonic potential energy for the protons, *J. Geophys. Res.*, *108*(A1), 1047, doi:10.1029/2002JA009487.

Lee, L. C. (2001), A new mechanism of coronal heating, *Space Sci. Rev.*, *95*, 95–106.

Lemaire, J., and V. Pierrard (2001), Kinetic models of solar and polar winds, *Astrophys. Space Sci.*, *277*, 169–180.

Lemaire, J. F., and V. Pierrard (2003), The kinetic treatment of space plasmas, *Rarefied Gas Dynamics: 23rd International Symposium*, edited by A. D. Ketsdever and E. P. Muntz, pp. 857–864, Am. Inst. of Phys., College Park, Md.

Lemaire, J., and M. Scherer (1971), Kinetic models of the solar wind, *J. Geophys. Res.*, *76*, 7479–7490.

Lemaire, J., and M. Scherer (1973), Kinetic models of the solar and polar winds, *Rev. Geophys.*, *2*, 427–468.

Liemohn, M. W., and G. V. Khazanov (1998), Collisionless plasma modelling in an arbitrary potential energy distribution, *Phys. Plasmas*, *5*, 580–589.

Lie-Svendsen, O., V. H. Hansteen, and E. Leer (1997), Kinetic electrons in high-speed solar wind streams: Formation of high-energy tails, *J. Geophys. Res.*, *102*, 4701–4718.

Maksimovic, M., V. Pierrard, and J. Lemaire (1997a), A kinetic model of the solar wind with Kappa distributions in the corona, *Astron. Astrophys.*, *324*, 725–734.

Maksimovic, M., V. Pierrard, and P. Riley (1997b), Ulysses electron distributions fitted with Kappa functions, *Geophys. Res. Lett.*, *24*, 1151–1154.

Meyer-Vernet, N. (2001), Large scale structure of planetary environments: The importance of not being Maxwellian, *Planet. Sp. Sci.*, *49*, 247–260.

Ogilvie, K. W., M. A. Coplan, and R. D. Zwickl (1982), Helium, hydrogen and oxygen velocities observed on ISEE3, *J. Geophys. Res.*, *87*, 7363–7369.

Parker, E. N. (1991), Heating solar coronal holes, *Astrophys. J.*, *372*, 719–727.

Phillips, J. L., and J. T. Gosling (1990), Radial evolution of solar wind electron distribution due to expansion and collisions, *J. Geophys. Res.*, *95*, 4217–4226.

Pierrard, V., and H. Lamy (2003), The effects of the velocity filtration mechanism on the heavy ions of the corona, *Sol. Phys.*, *216*, 47–58.

Pierrard, V., and J. Lemaire (1996), Lorentzian ion exosphere model, *J. Geophys. Res.*, *101*, 7923–7934.

Pierrard, V., M. Maksimovic, and J. Lemaire (1999), Electron velocity distribution function from the solar wind to the corona, *J. Geophys. Res.*, *104*, 17,021–17,032.

Pierrard, V., K. Issautier, N. Meyer-Vernet, and J. Lemaire (2001a), Collisionless model of the solar wind in a spiral magnetic field, *Geophys. Res. Lett.*, *28*, 223–226.

Pierrard, V., M. Maksimovic, and J. Lemaire (2001b), Self consistent kinetic model of solar wind electrons, *J. Geophys. Res.*, *107*, 29,305–29,312.

Schmid, J., P. Bochsler, and J. Geiss (1987), Velocity of iron ions in the solar wind, *J. Geophys. Res.*, *92*, 9901–9906.

Schwenn, R. (1990), Large-scale structure of the interplanetary medium, in *Physics of the Inner Heliosphere*, vol. 1, edited by R. Schwenn and E. Marsch, Springer-Verlag, New York.

Scudder, J. D. (1992a), On the causes of temperature change in inhomogeneous low-density astrophysical plasmas, *Astrophys. J.*, *398*, 299–318.

Scudder, J. D. (1992b), Why all stars possess circumstellar temperature inversions, *Astrophys. J.*, *398*, 319–349.

Tam, S. W. Y., and T. Chang (1999), Kinetic evolution and acceleration of the solar wind, *Geophys. Res. Lett.*, *26*, 3189–3192.

Treumann, R. A. (1999), Quantum statistical mechanics in the Lorentzian domain, *Europhys. Lett.*, *29*, 1–6.

Vocks, C., and E. Marsch (2001), A semi-kinetic model of wave-ion interaction in the solar corona, *Geophys. Res. Lett.*, *28*, 1917–1920.

von Steiger, R., J. Geiss, G. Gloeckler, and A. B. Galvin (1995), Kinetic properties of heavy ions in the solar wind from SWICS/ULYSSES, *Space Sci. Rev.*, *72*, 71–76.

Wimmer-Schweingruber, R. F., R. VonSteiger, J. Geiss, G. Gloeckler, F. M. Ipavich, and B. Wilken (1998), O^{5+} in high speed solar wind streams: SWICS/ULYSSES results, *Space Sci. Rev.*, *85*, 387–396.

Zouganelis, I., M. Maksimovic, N. Meyer-Vernet, H. Lamy, and V. Pierrard. (2003), A new exospheric model of the solar wind acceleration: the transsonic solutions, in *Solar Wind Ten*, edited by M. Velli et al., *AIP Conf. Proc.*, *679*, 315–318.

H. Lamy, J. Lemaire, and V. Pierrard, Belgian Institute for Space Aeronomy, 3 Avenue Circulaire, B-1180 Brussels, Belgium. (herve.lamy@oma.be; jfl@oma.be; viviane.pierrard@oma.be)